Non-linear MHD simulations of edge localized modes (ELMs)

Plasma Phys. Control. Fusion **51** (2009) 124012 (14pp) doi:10.1088/0741-3335/51/12/124012

Non-linear MHD simulations of edge localized modes (ELMs)

G T A Huysmans, S Pamela, E van der Plas and P Ramet[1]

CEA, IRFM, F-13108 Saint-Paul-lez-Durance, France
[1] LaBri, Université de Bordeaux I, Bordeaux, France

Received 19 June 2009, in final form 3 August 2009
Published 10 November 2009
Online at stacks.iop.org/PPCF/51/124012

Abstract
Non-linear MHD simulations of edge localized modes (ELMs) show features in qualitative agreement with the experimental observations such as the formation and speed of filaments, features in the radial profiles and the fine structure observed in the power deposition profiles at the divertor target. The density perturbation predominantly follows the ballooning mode convection cells leading to density filaments. The temperature perturbation, due to the large parallel conduction, follows the magnetic field perturbation. Simulations of pellets injected in the H-mode pedestal show that the high pressure in the high density plasmoid can become large enough to drive ballooning type modes forming a single helical structure located at the pellet (plasmoid) position.

(Some figures in this article are in colour only in the electronic version)

1. Introduction

Extrapolations of the edge localized mode (ELM) energy losses from current devices to ITER indicate that the expected ELM energy losses in ITER may be well above the acceptable limit to avoid fast material erosion of the first wall [1]. Current extrapolations are based on scaling of the ELM size with global parameters. To improve the ELM size predictions a more detailed understanding of the ELM physics is required. Direct numerical simulation can contribute to improve our physics understanding of ELMs and contribute to the interpretation of experimental results. In recent years, a large number of detailed fast measurements of the ELMs has become available. These measurements provide a good basis for the validation of the numerical simulation of ELMs.

In the first part of this paper, natural ELMs are simulated using the non-linear MHD code JOREK starting from the assumption that ELMs are ballooning mode instabilities driven by the pressure gradient in the H-mode pedestal. The non-linear evolution of density, temperature and current density profiles is discussed together with the associated density and energy losses. Also the convected energy losses at the divertor are considered.

In the second part of the paper, the plasma response to the injection of a pellet in an H-mode pedestal is studied. Pellets injected in the H-mode pedestal are known to trigger ELMs but the origin of the ELM trigger is still largely unknown. Non-linear MHD simulations of the evolution of an initial density perturbation in the pedestal can help clarify whether the pellet induced 3D perturbation can trigger ELMs or cause ELM-like MHD instabilities.

2. Non-linear MHD code JOREK

The non-linear MHD code JOREK solves the time evolution of the reduced MHD equations in general toroidal geometry. The magnetic field $\vec{B}$ and the velocity $\vec{v}$ are represented using the poloidal flux ψ and the electric potential u and the parallel velocity $v_\parallel$:

$$\vec{B} = (F_0/R)\vec{e}_\varphi + (1/R)\vec{\nabla}\psi(t) \times \vec{e}_\varphi \qquad \vec{v} = -R\vec{\nabla}u(t) \times \vec{e}_\varphi + v_\parallel(t)\vec{B}. \quad (1)$$

Substitution in the usual visco-resistive MHD equations including diffusive particle and heat transport yields the equations to be solved for the mass density ρ, temperature T, the perpendicular and parallel velocity and the poloidal flux:

$$\frac{\partial \rho}{\partial t} = -\nabla \cdot (\rho \vec{v}) + \nabla \cdot (D_\perp \nabla_\perp \rho) + S_\rho,$$

$$\rho \frac{\partial T}{\partial t} = -\rho v \cdot \nabla T - (\gamma - 1)\rho T \nabla \cdot v + \nabla \cdot (\kappa_\perp \nabla_\perp T + \kappa_\parallel \nabla_\parallel T + S_\mathrm{T},$$

$$\vec{e}_\varphi \cdot \nabla \times \left(\rho \frac{\partial \vec{v}}{\partial t} = -\rho(\vec{v} \cdot \vec{\nabla})\vec{v} - \vec{\nabla}(\rho T) + \vec{J} \times \vec{B} + \mu \Delta \vec{v} \right),$$

$$\vec{B} \cdot \left(\rho \frac{\partial \vec{v}}{\partial t} = -\rho(\vec{v} \cdot \vec{\nabla})\vec{v} - \vec{\nabla}(\rho T) + \vec{J} \times \vec{B} + \mu \Delta \vec{v} \right),$$

$$\frac{1}{R^2}\frac{\partial \psi}{\partial t} = \eta(T)\nabla \cdot \left(\frac{1}{R^2}\nabla_\perp \psi \right) - \vec{B} \cdot \nabla u, \quad (2)$$

$D_\perp$, $\kappa_\perp$ and $\kappa_\parallel$ are the perpendicular particle diffusion and the perpendicular and parallel heat conductivity, S_ρ and S_T represent the particle and heat source. $\eta(T) = \eta_0(T/T_0)^{-3/2}$ is the temperature dependent resistivity and μ is the viscosity. The equations are partly normalized using only $\mu_0\rho_0$. This means, for example, that the normalized time as used in this paper is $\tilde{t} = t/\sqrt{\mu_0\rho_0}$. The diffusion coefficients are normalized as $\tilde{D} = D\sqrt{\mu_0\rho_0}$ and the viscosity as $\tilde{\mu} = \mu\sqrt{\mu_0/\rho_0}$.

The boundary conditions are those of an ideally conducting wall (all perturbations set to zero) on the surfaces parallel to the magnetic field. On the open field lines, the parallel component of the velocity is set to the local sound speed in the outgoing direction (Mach-one condition) and a free outflow of density and temperature is applied. (The out-flowing density and heat are approximately compensated by the central heat and particle source.)

The JOREK code has been developed with the specific aim of simulating ELMs, i.e. to simulate ballooning modes and external kink (or peeling) modes located around the separatrix in X-point plasmas on open and closed field lines. To allow for an accurate representation of the variables, cubic 'Bezier' finite elements [2] are used in the poloidal plane. The Bezier elements are a generalization of the cubic Hermite elements (as used in the HELENA equilibrium code [3]). The Bezier elements are based on the so-called Bezier patches which are commonly used in computer aided design (CAD) applications. Using this representation both the variables and their derivatives are continuous. The (isoparametric) representation of the poloidal plane using the same finite elements allows an accurate alignment of the finite elements to the

equilibrium flux surfaces including the separatrix and x-point. The time stepping scheme in the JOREK code is fully implicit using the linearized Crank–Nicholson scheme on all the equations in one single step. The resulting large sparse matrices are solved using the direct parallel sparse matrix solver PastiX [4] and/or an iterative solver (GMRES) using the sub-matrices of each toroidal harmonic as an efficient pre-conditioner.

3. Non-linear MHD simulations of ELMs: ballooning modes

There is an increasing amount of evidence [5–8] that ELMs occur while the pressure gradient in the H-mode edge pedestal crosses the (ideal) MHD stability boundary for ballooning and external kink (peeling) modes. Linear MHD stability analysis of the H-mode pedestal with type I ELMs indicates that the pedestal is in the so-called second stable regime where the high-n modes are stabilized (due to the large edge bootstrap current and/or plasma shaping). The most unstable modes are ballooning or ballooning–peeling modes with medium-n toroidal mode numbers.

To investigate questions related to the ELM induced energy losses and the physics of the ELM cycle, non-linear MHD simulations [9–12] can provide physics insight and contribute to the interpretation of ELM observations. To determine the size of ELMs and the related ELM frequency, the MHD simulations should in principle include several consecutive ELMs. However, the simulation of several ELMs is extremely challenging due to the different timescales involved, from the fast crash timescale to the long recovery phase reheating the edge plasma. Simulations of multiple ELMs are slowly becoming feasible but, at present, the current status of non-linear MHD ELM simulations is to simulate one single ELM starting from an equilibrium unstable to medium-n ballooning modes. Obviously, this approach will not allow us to study how a plasma can become significantly unstable. It does allow us to investigate the dynamics of the ELM itself and (qualitative) comparison of the simulation results with the many detailed observations of the fast ELM events that have become available in recent years. Well-known examples are the fast camera observations of ELMs showing filamentary field-aligned structures being expelled from the plasma [13]. The same filaments are also seen in the mid-plane profiles of the density using fast Thomson scattering [13, 14]. The fine structure or stripes in the ELM induced heat flux observed on the divertor target [15] also provide detailed information on the ELM structure. The measurements can be used as a first step in the validation of the non-linear MHD simulation of ELMs.

The initial quasi-stationary equilibria are characterized by a large equilibrium flow just inside the separatrix due to the finite dissipation terms in the MHD model [9, 17–19]. In addition, there is a large parallel flow close to the target due to the applied Mach-one boundary condition. The stationary equilibria are obtained by first solving the static Grad–Shafranov equation on the open and closed field lines. This static axisymmetric solution is then evolved over typically 200 Alfven times such that the poloidal and parallel flows are well established. The flows and also the density and temperature profiles still evolve on their dissipation timescale which is typically much slower than the timescale of interest for the ELM crash. The H-mode edge pedestal is imposed by the shape of the initial profiles and by the radial profile of the particle and heat diffusivities which have a local minimum just inside the separatrix.

The simulations discussed below use a flux surface aligned mesh both on the open and closed field lines. The grid is radially refined at the separatrix and poloidally at the angle of the x-point. The number of cubic finite elements in the poloidal plane is about 9×10^3. In the toroidal direction, 8 Fourier harmonics are used with a periodicity of 3, i.e. the toroidal mode numbers range from $n = 0$ to $n = 21$. The non-linear terms are evaluated in real space on a grid of 32 planes (with a periodicity 3) in the toroidal direction. The total number of toroidal

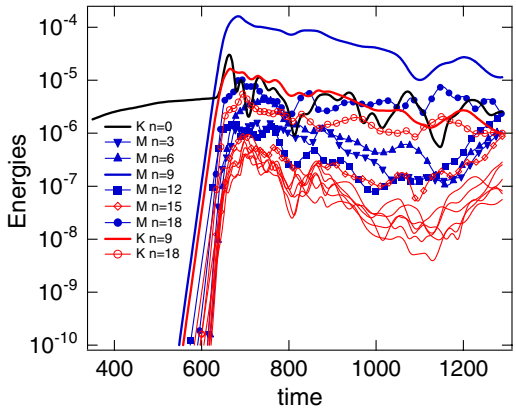

Figure 1. The magnetic (M) and kinetic energies (K) as a function of time for each toroidal harmonic.

harmonics and poloidal finite elements is limited due to the fully implicit numerical method and the corresponding computational requirements. (Note that the toroidal localization of modes with a high toroidal mode number may be limited due to the number of harmonics used). The total number of degrees of freedom, i.e. the size of the matrices to be solved at each time step, is of the order of 5×10^6.

The case discussed below is an example of a relatively large ELM. The JET-like equilibrium parameters are major radius $R_0 = 3.11$ m, minor radius $a = 0.87$ m, toroidal magnetic field $B_0 = 2.9$ T, current $I = 3.14$ MA, poloidal beta $\beta_p = 0.39$, normalized beta $\beta_N = 1.14$, q on axis $q_0 = 1.09$ and $q_{99} = 2.82$. The initial profiles of the density, temperature and toroidal current density are shown in figure 4. The pedestal width is ~4 cm in the outboard mid-plane. The amplitude of the edge current density is chosen such that the pedestal is in the so-called second stable regime where the high-n ballooning modes are stabilized. The initial equilibrium is marginally stable to an $n = 18$ ideal MHD ballooning mode. Including the resistivity $\eta(0) = 5 \times 10^{-6}$, the particle and heat diffusivities $D_\perp = 2 \times 10^{-5}$, $\kappa_\perp = 5 \times 10^{-6}$, $\kappa_\parallel = 10$ and the viscosities $\mu_\perp = 10^{-5}$, $\mu_\parallel = 10^{-5}$, the system is unstable to the modes $n =$ (6, 9, 12, 15, 18) with linear growth rates of (0.051, 0.069, 0.067, 0.066, 0.070). At the end of the long linear phase of exponential growth ($200\tau_A < t < 600\tau_A$), the dominant mode ($n = 9$) is determined by the initial noise level from which the modes start to grow. Figure 1 shows the evolution of the magnetic and kinetic energy of the individual toroidal harmonics.

The poloidal flow pattern of the linear ballooning mode structure has a radial half-width of about 5 cm inside the separatrix and 3 cm beyond the separatrix on the open field lines. This ballooning mode flow convects high density from the closed to the open field lines across the separatrix. At the same time low density is convected into the main plasma. The $n = 0$ poloidal flow, non-linearly induced by the ballooning mode [9], cuts the density perturbation from the main plasma, forming filaments of increased density. The low density interchanges with the high density to form the typical density profiles with a local maximum at the position of the filament.

Figure 2 shows a snapshot of the density in the poloidal plane at $t = 700\tau_A$ at which time the first density filaments have been formed. The density filaments are expelled on the low-field side. They then expand with the parallel velocity to the high-field side. The temperature is much less influenced by the poloidal flow due to the large parallel heat conduction which tends to keep the temperature constant on a field line. The magnetic perturbation is large enough to

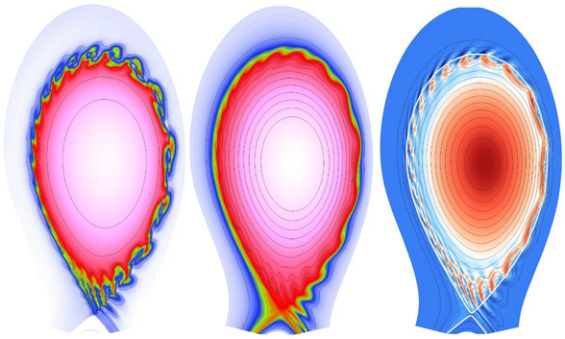

Figure 2. Density, temperature and toroidal current density in the poloidal plane at $t = 700\tau_A$.

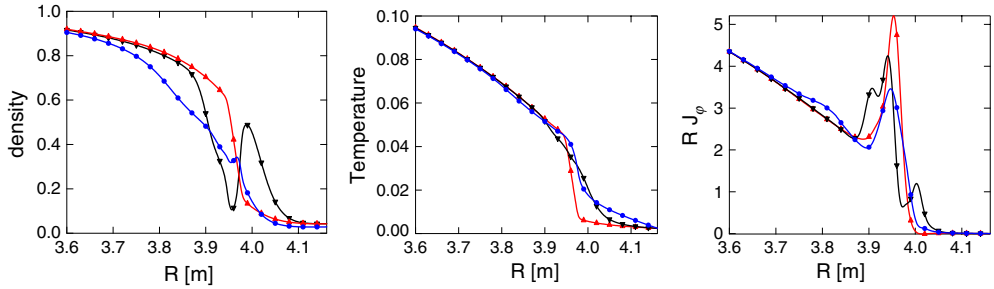

Figure 3. Density and temperature and toroidal current density in the outboard mid-plane at $t = 480\tau_A$ (red ▲), $t = 700\tau_A$ (black ▼) and $t = 1170\tau_A$ (blue ●).

cause a significant change to the equilibrium magnetic field structure. The Poincaré plot at the time of the maximum magnetic perturbation indicates an ergodic region with a width 2–3 times the pedestal width. Figure 5 shows a plot of the connection length of the field lines in a poloidal plane. There is still a relatively clear separation between field lines with a long connection length (inside the confined plasma) and shorter connection lengths outside. The separation between the two regions shows a ballooning-like perturbation. This same perturbation is visible on the temperature contours (see figure 2) illustrating that the temperature perturbations follow the magnetic field structure. On the low-field side, the toroidal current density also follows the magnetic structure, similar to the temperature. On the high-field side the current sheath in the pedestal is breaking up (figure 2, right).

Figure 3 shows the profiles of the density, temperature and the toroidal current density in the mid-plane for 3 time slices, at the start, at the maximum perturbation (as in figure 2) and at the end of the simulation. The density profile with a local minimum reflects the formation of density filament. The temperature profile remains monotonic due to the large parallel heat conduction. These profile shapes are in good qualitative agreement with the fast profile measurements in MAST [13] and JET [14]. The ELM affected area in the density profile ranges from $R = 3.7$–3.98 m, i.e. about 30% of the minor radius. The temperature losses are very small, the energy losses are predominantly convective. This may be due to the currently implemented divertor boundary conditions. These lead to the so-called 'simple' divertor solutions where the temperature along the field lines remains constant towards the target. This leads to very small parallel gradients and consequently small parallel conduction losses. The influence of the divertor conditions on the size of the temperature losses remains to be studied.

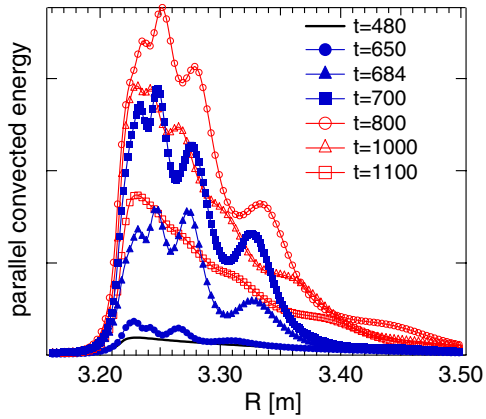

Figure 4. The parallel convected energy flux (in a.u.) to the outer target as a function of the major radius at the target for several time slices.

The non-linear saturation of the maximum ELM amplitude in this case is likely due to the reduction in the drive, i.e. the local pressure gradient, of the ballooning instability. The flux surface averaged edge pressure gradient is reduced by a factor of 2 at $t = 685\tau_A$ to a value well below the ideal MHD ballooning limit. Before the time of the maximum amplitude, the first density filaments have already been ejected from the main plasma. The non-linearly induced $n = 0$ flow from the first filaments has decayed. This allows the formation of a second set of larger filaments causing density losses deeper into the plasma. In general, the interaction of the medium-n ballooning mode with the $n = 0$ poloidal flow (by the non-linearly induced flow but also the equilibrium flow) is an important characteristic of the non-linear dynamics of the ELM simulations. The flux surface averaged current density in the edge pedestal remains large and is reduced by only 15%. After the maximum perturbation, there is a slow decay (slow compared with the linear growth rates) of the magnetic and kinetic perturbations. During this phase there is still an increased level of energy and density losses from the main plasma. In this case, the total energy loss from the main plasma is 7% of the total thermal energy, the total density loss is 10%, the total current loss is less than 1%.

3.1. Fine structure on the power deposition profiles

The current MHD model used in the simulations, including the parallel velocity and the Mach-one boundary condition at the target, is a first step towards a more complete description of the solution in the divertor. The model allows a first look at the energy deposition profiles at the target. Figure 4 shows the convected energy at the outer target at several time slices. During this simulated ELM the peak convected energy flux exceeds the pre-ELM flux by a factor of 20. The energy deposition profile on the outer target shows a fine structure on top of the usual radially decaying profile. The radial size of the structures is about 1–2 cm becoming wider going from the separatrix towards the outside. The structures are mostly due to the temperature profile variations but somewhat broader structures are also seen on the density profile at the target. In the toroidal direction these structures form spirals with the periodicity of the toroidal mode number ($n = 9$) of the dominant ballooning mode instability. Figure 6 shows a poloidal cut of the temperature profile and the plasma temperature at the target illustrating the connection between the structures in the poloidal plane and the spirals in the toroidal direction.

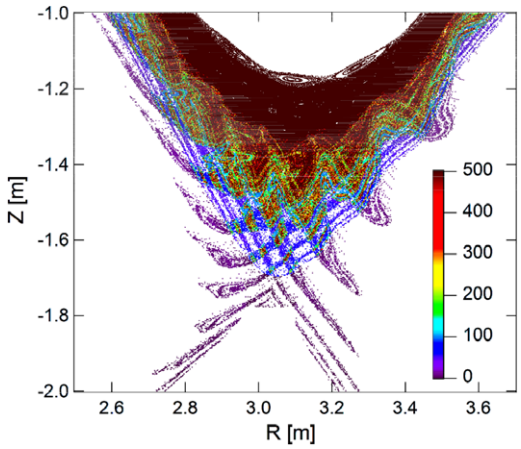

Figure 5. The connection length for field lines starting inside the unperturbed separatrix at $t = 684\tau_A$.

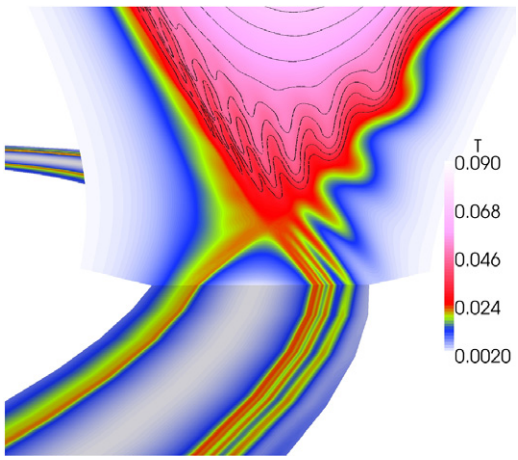

Figure 6. A poloidal and toroidal cut of the plasma temperature at $t = 684\tau_A$ showing the ELM induced stripes/spirals on the target.

On the inner target, a very faint fine structure in the temperature can be observed but with a much smaller amplitude and smaller number of stripes.

The origin of the structures can be understood from the topology of the magnetic field, perturbed by the magnetic perturbation of the ballooning mode. Figure 5 shows a poloidal map of the connection length of field lines to the nearest target for field lines that originated inside the (unperturbed) separatrix. In the mid-plane the magnetic perturbation shows the typical ballooning perturbation. The field lines escaping from the main plasma (due to the ergodic plasma edge) are connected to the target.

The poloidally elongated ballooning mode structures in the mid-plane are deformed into radially elongated and poloidally localized structure at the target. This deformation is due to the equilibrium magnetic field structure in the presence of an x-point. The temperature perturbations reflect these magnetic structures due to the high parallel heat conduction. The broadening of the stripes away from the separatrix is also a consequence of the magnetic field line structure.

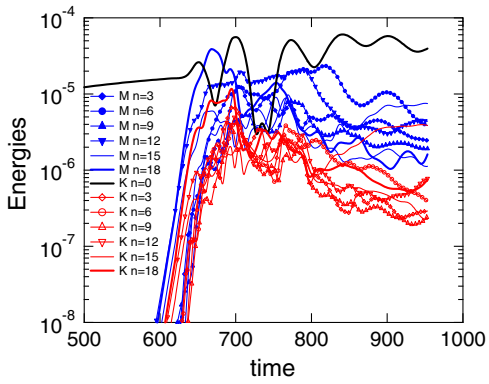

Figure 7. The time evolution of the magnetic (M) and kinetic energies (K) for each of the toroidal harmonics for a medium size ELM.

It should be noted that very similar patterns will be observed in the case of a ballooning-like temperature perturbation crossing the unperturbed separatrix conducted to the target following the equilibrium magnetic field [15, 16].

That fewer stripes are observed on the inner target may be related to the fact that the lobes of the 'lost' field lines below the x-point tend to curve away from the separatrix on the inboard side (see figure 5). As a consequence, the spacing between the stripes will quickly become much larger away from the separatrix (as compared with the outer target).

The fine structure in the convected power flux to the target during the ELM simulation is qualitatively in good agreement with the experimentally observed substructure (stripes) on the outer target during ELMs in AUG [15, 16] and JET [20].

3.2. ELM size versus linear mode width

To compare the ELM size and ELM affected area with respect to the width of the linear mode structure, the large ELM case described above is compared with a similar case where the most unstable mode has a narrower linear mode structure. The parameters for this case are $\beta_p = 0.63$, $\beta_N = 1.8$, $\eta(0) = 10^{-6}$, $D_\perp = 10^{-5}$, $\kappa_\perp = 5 \times 10^{-6}$, $\kappa_\parallel = 10$, $\mu_\perp = 10^{-5}$ and $\mu_\parallel = 10^{-4}$. The pedestal width is identical to the large ($n = 9$) ELM case described above. The pressure at the top of the pedestal is about 25% higher such that the linear growth rates are comparable to the large ELM case. The magnetic and kinetic energy evolution of the toroidal harmonics for this case is shown in figure 7. The linear growth rates for the unstable modes $n = (6, 9, 12, 15, 18, 21)$ are (0.044, 0.060, 0.067, 0073, 0.067). In this case, in the linear and early non-linear phase the $n = 18$ harmonic is the most unstable mode. The exact reason why the $n = 18$ is dominant is difficult to establish. The reduced radial width of the mode is due to the higher toroidal mode number. After the early non-linear phase, the mode number of the largest mode evolves to lower toroidal mode numbers. The maximum amplitude of the magnetic perturbation is much smaller compared with the large ($n = 9$) ELM case. The maximum kinetic energy is of comparable amplitude.

Comparing the width of the linear eigenmode (see figure 8) with the perturbed density profiles shows a strong correlation between the eigenmode width, the width of the density filament and the ELM affected area at this time. This is not too surprising since the width of the eigenmode determines the radial width of the convective cells that create the density filaments. However, in the later non-linear phase, the ELM affected area increases from about

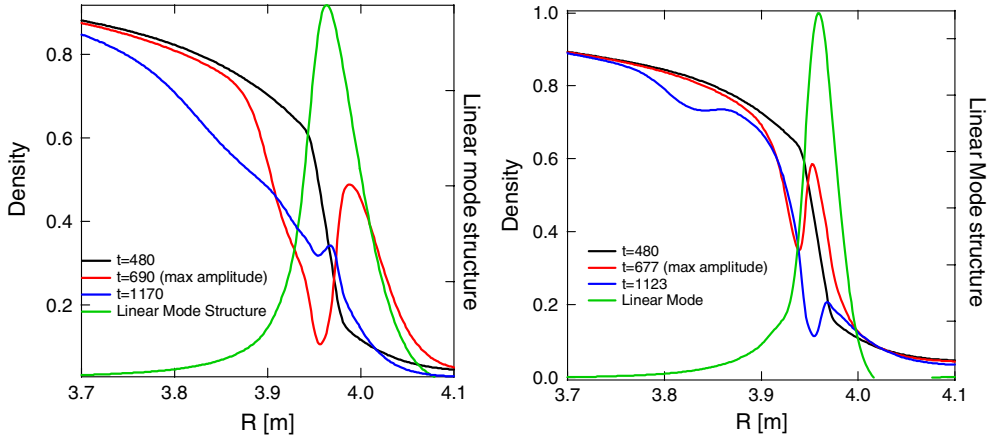

Figure 8. The density profiles at the start, at the maximum perturbation and at the end of the simulation compared with the mode structure of the velocity in the linear phase for the large (middle) and medium (right) size ELM.

10 to 30 cm for the large ($n = 9$) ELM case. In the medium ($n = 18$) ELM case, the density losses do not penetrate deeply into the plasma (up to 15 cm). The different behaviour may be due to the difference in the poloidal rotation, which is much stronger in the medium size ($n = 18$) ELM case. The stronger poloidal flow may prevent the formation of radially more elongated convection cells. Since the dominant loss mechanism is by convection, the ELM affected area is very similar for the thermal energy losses.

4. Plasma response to 'pellets' in the H-mode pedestal

One promising option to control the ELM frequency, and thereby the energy loss per ELM, is by pellet injection. In AUG it was shown [21] that the ELM frequency can be controlled using pellet injection. It was observed [21, 22] that the injection of a pellet in an H-mode plasma can trigger an ELM during any phase of the periods in between natural ELMs, even very shortly after the occurrence of a natural ELM. The amplitude of the pellet induced ELM is similar to the amplitude of a natural ELM when compared at the same ELM frequency. Also the amplitude and the rise time of the magnetic perturbation is of the same order but generally larger for the pellet induced ELM [26]. Injection of a pellet in Ohmic, L-mode and QH-mode plasmas also yields a (smaller) magnetic perturbation but not an ELM-like event [23]. In AUG it was shown that the ELM is triggered when the pellet reaches the middle of the transport barrier, independent of the velocity and mass of the pellet [25].

The trigger of the ELM by a pellet during any phase of the ELM period might be troublesome for the common interpretation of the ELM onset, namely, the crossing of the ideal MHD stability boundary for ballooning (and/or peeling) modes [28, 29]. It could imply that the plasma edge is always non-linearly unstable and only requires a trigger to produce an ELM (similar to the trigger of neo-classical tearing modes [24]. However this argument ignores the influence of the pellet on the plasma. Alternatively, instead of being a trigger, the pellet could be the cause of the ELM by pushing the plasma beyond the relevant MHD stability limit. The pellet can create a local field-aligned plasmoid which can have a local pressure exceeding the plasma pressure. In this non-axisymmetric configuration with a non-stationary local pressure perturbation, the ideal MHD stability limits of the original axisymmetric equilibrium may

not be very relevant. Early non-linear MHD simulations [27] of the influence of pellets (in the framework of pellet induced disruptions) have indicated that the pellet induced pressure perturbation can destabilize ballooning modes. In [23] it is proposed that the pellet plasmoid pressure is a candidate for the trigger (or better, the cause) of the ELM.

In this section, the influence of a pellet injected in an H-mode-like edge pedestal is studied in the framework of non-linear MHD using the code JOREK. The pellet is modelled as a large-amplitude, localized, (initially) static density perturbation. This density perturbation is added to a plasma in equilibrium while keeping the pressure profile unchanged (pellets only provide density not energy). This leads to an initial state with a localized minimum in the temperature profile. The initial state is still in magnetic equilibrium, satisfying the force balance. This initial state with a density and temperature perturbation is subsequently evolved in time using the reduced MHD model as described above.

In the non-linear MHD simulations presented here, toroidal harmonics ranging from $n = 0$ to $n = 10$ are used. The choice of toroidal mode numbers limits the localization in the toroidal direction of the initial density (and temperature) perturbation. The full-width half maximum of the density perturbation is about 16% of the toroidal circumference.

To simplify the initial studies of the plasma response to the 'pellet' perturbations, we start with a circular plasma shape. The unperturbed density and temperature profile are characterized by a large gradient at the plasma boundary (see figure 10(*b*)) mimicking the H-mode edge pedestal. The edge pressure gradient is chosen such that the plasma without pellet perturbation is stable to ballooning modes (in the range of toroidal mode numbers $n = 1$–10). Other parameters of the simulation are major radius $R_0 = 3.0\,\mathrm{m}$, minor radius $a = 1.0\,\mathrm{m}$, toroidal magnetic field $B_0 = 3\,\mathrm{T}$, toroidal current $I = 1.2\,\mathrm{MA}$, poloidal beta $\beta_\mathrm{p} = 0.84$, toroidal beta $\beta = 0.56\%$, q on axis $q_0 = 1.84$, q at the boundary $q_1 = 3.1$, the resistivity on axis $\eta(0) = 10^{-6}$, viscosity $\mu = 10^{-5}$, perpendicular particle diffusivity $D_\perp = 2 \times 10^{-5}$, perpendicular heat diffusivity $\kappa_\perp = 2 \times 10^{-5}$ and parallel heat conductivity $\kappa_\parallel = 50$.

In the initial state the density perturbation has a maximum amplitude of 25 times the background density, the pellet radius in the poloidal plane is chosen at 8% of the minor radius. The total added number of particles is 6% of the initial particle content. To be able to resolve the very large local gradients due to the local pellet perturbation, a radially and poloidally refined grid of finite elements is used with 51 radial and 96 poloidal cubic finite elements.

Figure 9 shows four frames from the evolution of the density, plasma flow (contours of the electric potential), temperature and current density from the non-linear MHD simulation. The first column shows the initial state. The hole in the temperature is very quickly filled up due to the very large parallel conduction while the density evolves on a slower timescale with the parallel velocity. This results in a local region with a strongly increased pressure. This in turn drives an electric field perturbation (the contours in the density plots) which leads to the well-known [27] $v_\perp = E \times B$ drift of the pellet density radially outwards for pellets injected on the low-field side.

The evolution of the pressure maximum is shown in figure 10(*b*). The pressure increases within a few Alfven times to a value 6 times the pressure on axis in a region slightly larger than the size of the original pellet perturbation. The local pressure in 'plasmoid' decays in a few tens of Alfven times due to the parallel flow induced by the large parallel pressure gradient. In the initial phase ($0 < t < 10\tau_\mathrm{A}$) the pressure maximum is located at the original pellet position in the outer mid-plane. Afterwards, the density perturbation splits into two parts spreading along the field lines with the parallel velocity. The pressure maximum moves with the density perturbation. As the density maximum moves around poloidally and radially inwards, the pressure inside the plasmoid increases slowly. In this phase ($t > 10\tau_\mathrm{A}$) the pressure maximum

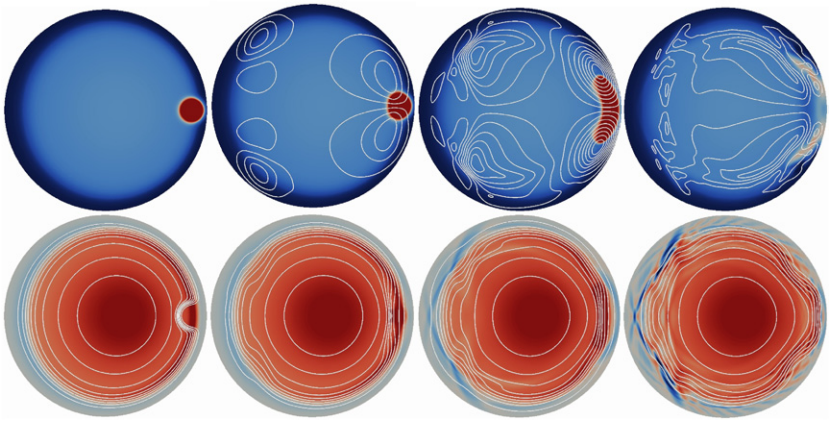

Figure 9. The evolution of the plasma density (top, colour), the velocity flow lines (equi-potential lines) (top, contours), the current density (bottom, colour) and temperature contours (bottom, contours) at $t = 0$, 6, 10 and 26 τ_A.

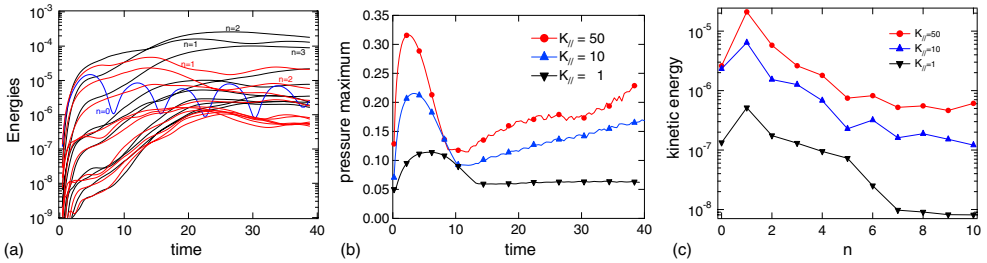

Figure 10. (*a*) The evolution of the magnetic (black) and kinetic (red) energies for each toroidal harmonic as a function of time due to a 'pellet' perturbation at $t = 0$ for $\kappa_{\|} = 50$. (*b*) The maximum pressure as a function of time for different parallel heat conduction coefficients $\kappa_{\|} = 1$, 10, 50. (*c*) The kinetic energy perturbation as a function of the toroidal mode number at the maximum perturbation for three values of the parallel conductivity $\kappa_{\|} = 1$, 10, 50.

has moved away from the 'bad' curvature region. However, the localized pressure perturbation has both negative and positive gradients (radially). Thus, even in the good curvature region ballooning modes could in principle be destabilized at the radii where the pressure gradient is positive.

The evolution of the magnetic and kinetic energies of the individual toroidal harmonics is shown in figure 10(*a*). There is a very fast initial response corresponding to the fast pressure rise in the plasmoid and the loss of the initial equilibrium. In this first phase the growth of the perturbations is dominated by the low-n ($n = 1$, 2) harmonics. In a second phase, there is a fast growth of all the harmonics including the higher-n harmonics. The mode structure of the toroidal modes shows a typical structure of a ballooning mode. All the toroidal harmonics are coupled to form a single helical structure located on (and around) the pellet position. The ballooning perturbation is clearly visible in the temperature contours bulging outwards (see figure 9). Figure 11(*a*) shows the 3D helical structure of the temperature perturbation on a flux surface (at $t = 26\tau_A$). By this time the density perturbation has split into two parts slowly spreading along the magnetic field (see the yellow contours in figure 11(*a*)). The amplitude

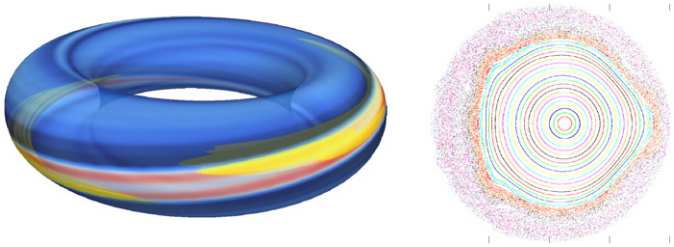

Figure 11. (*a*) The temperature on a flux surface at $t = 26\tau_A$ showing a single helical ballooning type perturbation (colour scale from blue, $T = 6 \times 10^{-3}$ to red, $T = 8 \times 10^{-3}$). Also shown (in yellow) is the density contour at twice the central density. (*b*) The Poincaré plot (at $t = 26\tau_A$) of the magnetic field showing an ergodic region at the position of the pellet perturbation.

of the magnetic perturbation is large enough to ergodize the flux surfaces where the pellet was 'deposited'. This is illustrated in figure 11(*b*) showing a Poincaré plot of the magnetic field.

The simulation has been repeated with smaller values for the parallel conduction $\kappa_\parallel = 10$ and $\kappa_\parallel = 1$. The resulting evolution of the pressure maxima is included in figure 10(*b*). It clearly shows the importance of the parallel conduction, relative to the parallel velocity, in the formation of the high pressure plasmoid. As a consequence of the lower plasmoid pressure, the growth rates of the ballooning type modes are reduced and the helical perturbation grows to a much smaller amplitude. Figure 10(*c*) shows the toroidal mode number spectrum of the kinetic energy perturbation for the three values of the parallel conductivity. The amplitude of the magnetic energy perturbation is reduced by about a factor of 2 for $\kappa_\parallel = 10$ as compared with the $\kappa_\parallel = 50$. For $\kappa_\parallel = 1$, the amplitude is reduced by a further factor of 10.

For a first investigation on the plasma response in an x-point plasma with an H-mode-like edge pedestal and to see if an ELM-like instability can be created, a pellet density perturbation is added just inside the separatrix. The density perturbation has a radius of 8% of the minor radius and an amplitude of 25 times the central density. This increases the total particle content by 3%. Before the pellet perturbation is added, the equilibrium has been evolved to a quasi-stationary state with parallel and perpendicular equilibrium flows. The equilibrium is characterized by $R_0 = 3.1\,\mathrm{m}$, $B_0 = 1\,\mathrm{T}$, $a = 0.72\,\mathrm{m}$, $\beta_p = 0.84$, $\beta_N = 1.89$, $q_0 = 1.0$ and $q_{99} = 3.7$. Other parameters are $\eta(0) = 10^{-6}$, $\kappa_\parallel = 10$, $\kappa_\perp = 2 \times 10^{-6}$, $D_\perp = 2 \times 10^{-6}$ and $\mu = 5 \times 10^{-6}$. In this case the grid comprises 7750 cubic finite elements refined radially around the separatrix and poloidally at the pellet position and the x-point position.

The general behaviour in the x-point plasma is very similar to that described above for the circular plasma. A strong pressure develops in the high density plasmoid, in this case the maximum pressure is ~5 times the pressure on axis. Also in this case, there is a strong initial growth of the low-n modes followed by a growth phase of the higher-n modes ballooning-like modes. The evolution of the magnetic and kinetic energy for each toroidal harmonic is shown in figure 12. The coupled toroidal harmonics lead to one single helical perturbation centred on the field line of the original pellet position. Initially the maximum perturbation grows in the outer mid-plane. Later in the evolution the maximum perturbation moves with the density perturbation and the corresponding pressure maximum to the top of the plasma. This is illustrated in figure 13 showing the helical perturbation to the temperature on a flux surface just inside the separatrix at $t = 330\tau_A$. At this time the outer 25% of minor radius of the plasma is ergodized.

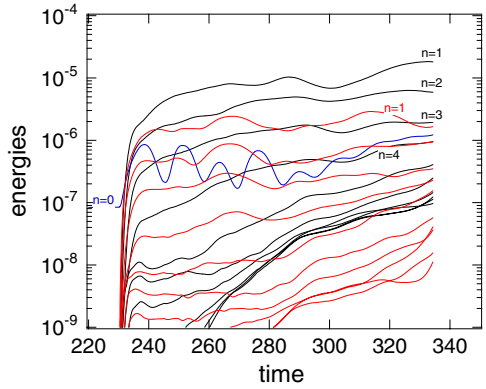

Figure 12. The evolution of the magnetic (black) and kinetic (red) energy for each toroidal harmonic ($n = 0, 10$).

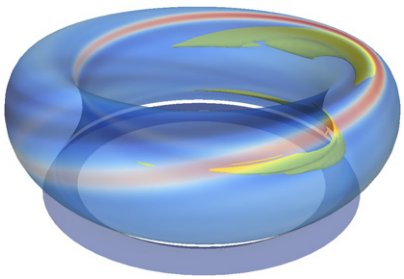

Figure 13. The temperature on a flux surface just inside the separatrix ($8 \times 10^{-4} < T < 2 \times 10^{-3}$) at $t = 330\tau_A$. The density contour of twice the central density is shown in yellow. The initial density perturbation was injected in the pedestal on the left-hand side (in the figure).

5. Conclusion

The non-linear MHD simulations of ballooning modes in the H-mode edge pedestal show the formation of density filaments expelled across the separatrix. These filaments show up in the mid-plane density profiles capturing the interchange of low density from outside the separatrix with high density from inside following the ballooning mode convective cells. The temperature profile in the pedestal remains monotonically decreasing but does show the ballooning mode deformation on the low-field side. The resulting profiles are in qualitative agreement with the fast profile measurements during the ELMs. Due to the high parallel energy conduction, the temperature follows the perturbed magnetic field lines. One observable consequence of this is the formation of a fine structure with a typical size of the order of 1 cm of the convected energy flux to the divertor target. Very similar structures have been observed experimentally in the heat deposition profiles in JET, AUG and MAST.

Simulations of pellets injected in the H-mode pedestal show that the high pressure in the high density plasmoid can become large enough to drive ballooning type modes forming a single helical structure located at the pellet (plasmoid) position. This indicates that the pellet may not just be a trigger to the ELM but that the 3D pellet perturbation can drive the plasma unstable to ballooning modes.

Acknowledgment

This work, supported by the European Communities under the contract of Association between EURATOM and CEA, was carried out as part of the project ANR-CIS.2006.01 and has benefited from financial support from the French 'Agence National de la Recherche'. The views and opinions expressed herein do not necessarily reflect those of the European Commission.

Stimulating discussions with M Becoulet, B Pegourie, A Kirk, M Beurskens, T Eich, R Wenninger, W Fundamenski, F Poli, G Arnoux and A Alonso are gratefully acknowledged.

References

[1] Loarte A *et al* 2003 *Plasma Phys. Control. Fusion* **45** 1549
[2] Czarny O and Huysmans G 2008 *J. Comput. Phys.* **227** 7423–45
[3] Huysmans G T A *et al* 1991 *Proc. CP90—Conf. on Computational Physics (Amsterdam)* (Singapore: World Scientific) p 371
[4] Hénon P, Ramet P and Roman J 2008 *Parallel Comput.* **34** 345–62
[5] Snyder P B *et al* 2004 *Nucl. Fusion* **44** 320
[6] Snyder P B *et al* 2007 *Nucl. Fusion* **47** 961
[7] Saarelma S *et al* 2007 *Plasma Phys. Control. Fusion* **49** 31–42
[8] Saarelma S *et al* 2009 *Plasma Phys. Control. Fusion* **51** 035001
[9] Huysmans G T A and Czarny O 2007 *Nucl. Fusion* **47** 659–66
[10] Strauss H R *et al* 2006 *Proc. 21st Int. Conf. on Fusion Energy 2006 (Chengdu, China, 2006)*
[11] Pankin A *et al* 2007 *Plasma Phys. Control. Fusion* **49** S63–S75
[12] Mizuguchi N *et al* 2007 *Nucl. Fusion* **47** 579–85
[13] Kirk A *et al* 2006 *Phys. Rev. Lett.* **96** 185001
[14] Beurskens M N A *et al* 2008 *Proc. 22nd Int. Conf. on Fusion Energy 2008 (Geneva, Switzerland, 2008)*
[15] Eich T *et al* 2003 *Phys. Rev. Lett.* **91** 195003
[16] Eich T *et al* 2005 *Plasma Phys. Control. Fusion* **47** 815–42
[17] Strauss H R 1995 *Phys. Plasmas* **2** 1229
[18] Pamela S *et al* 2008 Theory of fusion plasmas *AIP Conf. Proc.* **1069** 318–24
[19] Aydemir A Y *et al* 2007 *Phys. Plasmas* **14** 056118
[20] Devaux S *et al* 2009 *36th EPS Conf. on Plasma Physics (Sofia, Bulgaria)*
[21] Lang P T *et al* 2003 *Nucl. Fusion* **43** 1110–20
[22] Lang P T *et al* 2007 *Nucl. Fusion* **47** 754–61
[23] Lang P T *et al* 2008 *Nucl. Fusion* **48** 095007
[24] Lang P T *et al* 2008 *Plasma Phys. Rep.* **34** 711–5
[25] Kocsis G *et al* 2007 *Nucl. Fusion* **47** 1166–75
[26] Neuhauser J *et al* 2008 *Nucl. Fusion* **48** 045005
[27] Strauss H and Park W 1998 *Phys. Plasmas* **5** 2676
[28] Wilson H R *et al* 2006 *Plasma Phys. Control. Fusion* **48** A71–A84
[29] Huysmans G T A 2005 *Plasma Phys. Control. Fusion* **47** B165–78